Steel and Composite Structures, *Vol. 31, No. 5 (2019) 437-452*
DOI: https://doi.org/10.12989/scs.2019.31.5.437

Research on static and dynamic behaviors of PC track beam for straddle monorail transit system

Yongqing Yang [1a], Deng Yang [1b], Hongye Gou [*1] and Yi Bao [2c]

[1] *Department of Bridge Engineering, School of Civil Engineering, Southwest Jiaotong University, Chengdu 610031, China*
[2] *Department of Civil, Environmental and Ocean Engineering, Stevens Institute of Technology, Hoboken, NJ 07030, USA*

(*Received May 13, 2018, Revised March 28, 2019, Accepted April 19, 2019*)

Abstract. In this study, in-situ static and dynamic tests of four pre-stressed concrete (PC) track beams with different span lengths and curvatures in a straddle monorail transit system were reported. In the static load tests, the strain and deflection at critical sections of the PC track beams were measured to determine the load bearing capacity and stiffness. The dynamic responses of strain, deflection, acceleration, and displacement at key positions of the PC track beams were measured under different train speeds and train loads to systematically study the dynamic behaviors of the PC track beams. A three-dimensional finite element model of the track beam-vehicle coupled vibration system was established to help understand the dynamic behavior of the system, and the model was verified using the test results. The research results show that the curvature, span length, train speed, and train loads have significant influence on the dynamic responses of the PC track beams. The dynamic performance of the PC track beams in the curve section is susceptible to dynamic loads. Appropriate train loads can effectively reduce the impact of the train on the PC track beam. The PC track beams allow good riding comfort.

Keywords: straddle monorail; PC track beam; in-situ static and dynamic tests; finite element; coupled vibration; dynamic responses; riding comfort

1. Introduction

With the increase of urban traffic congestion and environmental pollution, a straddle monorail transportation system has attracted worldwide attention recently (Goda *et al*. 2000, Lee *et al*. 2005). As a new type of structure for urban short-distance transportation, the straddle monorail system has many significant advantages including less occupied land, negligible influence on existing ground transportation, strong terrain adaptability, low noise, etc. (Naeimi *et al*. 2014). Therefore, the straddle monorail system is considered to be effective in alleviating urban traffic pressure (Wang *et al*. 2018). In some cities, it has achieved rapid development, such as in Tokyo and Chongqing (Lee *et al*. 2006, Zhong and Zhu 2013).

Compared with conventional railways with steel wheel-rail system, the straddle monorail system has a different running mechanism: the train has rubber tires, and firmly grasps the track beams through traveling wheels, guide wheels, and stable wheels (Wang 2004), making the monorail system less noisy and more stable (Lee *et al*. 2005, Kim and Kawatani 2006). The track beam is not only a load-bearing component but also a path-guiding component (Wang 2004, Liu *et al*. 2010). When a train runs on the track beam, the train has a dynamic impact on the bridge and stimulates the bridge to vibrate. In turn, the vibration of the bridge increases the vibration of the train, resulting in a complex multi-degree-of-freedom vibration system (Gou *et al*. 2018a, b). It is worth noting that the coupled vibration between the train and the track beam often amplifies the dynamic response of the monorail system, affecting the safety and comfort of the train (Gou *et al*. 2018c). Curved track beam is subjected to coupled bending-torsion effect under the train load, so the coupling effect of the vehicle-bridge may be magnified compared with straight track beam (Shan and Li 2004, Huang *et al*. 2010, Song *et al*. 2012).

In the last two decades, a limited number of studies have reported the dynamic mechanism of straddle monorail bridges under moving trains. Lee *et al*. (2005) idealized a train model with 15 degrees of freedom (DOFs) to investigate the dynamic behaviors of vertical settlement, nodding, head shaking, side-rolling, and yawing. A train-bridge coupled analytical procedure based on the Lagrange's formulation was proposed to investigate the dynamic response of the straight steel-concrete composite monorail bridge under moving trains. Lee *et al*. (2006) used the same method to investigate the dynamic performance of the train-bridge coupling of a straight simple-supported steel bridge. Ivanchenko (2008) presented a theoretical method for dynamic analysis of monorail structures. Naeimi *et al*. (2014) developed an innovative model of train-beam interaction based on the multi-body dynamics (MBD) and finite element (FE) method to assess the dynamic behavior of monorail-bridge system. In order to investigate dynamic

*Corresponding author, Ph.D., Associate Professor,
E-mail: gouhongye@swjtu.edu.cn
[a] Professor, E-mail: yangyongqingx@163.com
[b] Ph.D. Student, E-mail: yangdeng1214@163.com
[c] Assistant Professor, E-mail: yi.bao@stevens.edu

ISSN: 1229-9367 (Print), 1598-6233 (Online)

interactions of the coupled system in the vertical and longitudinal directions, Naeimi *et al*. (2015) established a FE model of the straight bridge under monorail train loading. Kim *et al*. (Kim and Kawatani 2006, Kim *et al*. 2013) analyzed the dynamic effect of trains on steel monorail bridges under moderate or strong earthquakes based on the MBD method and three-dimensional (3D) dynamic response analysis. Recently, Wang *et al*. (2018) assumed each vehicle of monorail train as an MBD system with 18 DOFs and proposed a dynamic response analysis method of monorail bridge-train interaction system considering slip effect. Most of the existing studies, if not all, are mainly based on analytical and numerical methods. To date, there remains lack of experimental data, especially for pre-stressed concrete (PC) track beams. Because of the assumptions and idealizations of the bridge and trains in the analytical and numerical methods, the computational models may not represent the realistic conditions of a complex train-bridge system. In addition, due to excellent mechanical properties and good braking performance (Lee *et al*. 2005, Kim *et al*. 2013), PC track beams are one of the most important components in a straddle monorail transportation system (Zhong and Zhu 2013). Therefore, it is particularly important to investigate the static and dynamic behaviors of the PC track beam to ensure the safety of the straddle monorail traffic and riding comfort of the train.

Model test and in-situ test are effective in investigating the mechanical performance of bridge structures (Peng *et al*. 2016, Votsis *et al*. 2017, Gou *et al*. 2018d, e), The test data can be used to validate the finite element models (Gou *et al*. 2018f, g, 2019, Cui *et al*. 2018a, b). A field test was conducted to investigate the dynamic characteristics of a 27-m, three-span, concrete bridge (Hogan *et al*. 2016). The seismic performance of bridges was investigated through experiments (Altunisik and Kalkan 2016, Peng *et al*. 2016, Toydemir *et al*. 2017). Static and dynamic tests were performed to understand the actual behavior of a railway bridge that spans Karakaya Dam Lake between the cities of Malatya and Elazig in Turkey (Caglayan *et al*. 2015). The dynamic responses of the strain, acceleration, and displacement of continuous railway bridges were tested in situ (Gou *et al*. 2018a). Gou *et al*. (2018b) studied the dynamic responses of an asymmetrical arch railway bridge under moving trains. Based on in-situ loading tests, the dynamic behaviors of the world's longest steel box tied-arch bridge were studied (Gou *et al*. 2018c). The dynamic responses of a 77-year-old single-span steel truss railway bridge were determined by field measurements, modal analysis, and a generalized single DOF analysis (Shibeshi and Roth 2016). Based on the in-situ loading test, Song *et al*. (2017) analyzed the natural frequencies, accelerations, and displacements of the curved bridge structure under moving vehicles.

This paper investigates the static and dynamic behaviors of the PC track beam in a straddle monorail system through in-situ loading tests. Four PC track beams with different curvatures and span lengths were tested. The static deflection and strain of the beam were measured in static load tests to determine the static behavior of each PC track beam. The investigated dynamic responses include the free vibration characteristics, strains, deflections, torsion angles, displacements, accelerations, and dynamic amplification factors. Based on experimental data, correlations between various dynamic responses and calculated spans, train loads, train speeds were investigated, and the influence of curvature radius on the dynamic response of track beams was analyzed. Three-dimensional finite element models of a PC monorail simple-supported beam bridge and a vehicle were established to analyze the coupled dynamics of the train-bridge system.

Table 1 Designation and span of the PC track beams

PC track beams	Straight line	Transition curve		Round curve (R = 60 m)
Designation	TB01	TB02	TB03	TB04
Span length (L)	23.2 m	19.2 m	15.9 m	17.235 m

2. Description of PC track beams

The maximum design speed of monorail trains is 80 km/h. Four PC track beams of three different planar arrangements were selected. The line types of these three typical intervals are straight lines (TB01), transition curves (TB02 and TB03) and round curves (TB04), respectively, as shown in Table 1. The radius of the round curve is 60 m. The transition curve is between the straight line and the round curve with a radius of 400 m. The track beam TB01is shown in Figs. 1(a) and (b).

The four PC track beams have the same cross section:

(1) The four PC track beams have rectangular box cross sections with a width of 0.7 m and a height of 1.5 m.
(2) Both ends of each beam have a solid cross section with a length of 1.7 m, and one lateral diaphragm with a thickness of 0.2 m at the mid-span.
(3) The roof thickness at the mid-span of the beam is 0.215 m, the soleplate thickness is 0.205 m, and the web thickness is 0.22 m.
(4) The thicknesses of the web and soleplate changes linearly from the solid section to the hollow section.
(5) The maximum thicknesses of the web and soleplate are 0.455 m and 0.275m, respectively.

3. In-situ experimental program

3.1 Test plan

Static and dynamic load tests were conducted on the four PC track beams. For the static load tests, the static strain and displacement of each track beam were investigated to evaluate their working status under static loading. In the dynamic load tests, ambient vibration tests and train loading tests were carried out on each track beam.

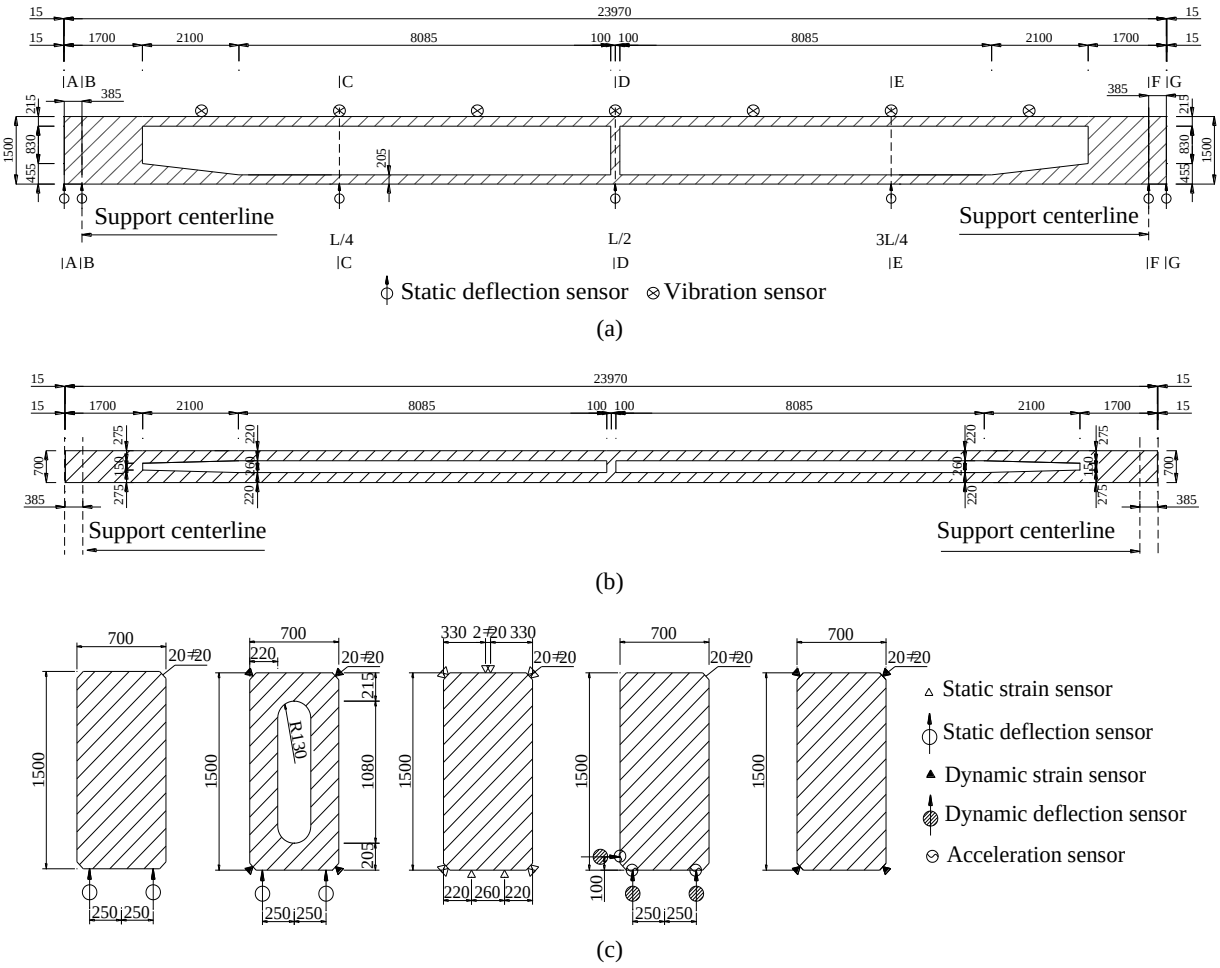

Fig. 1 PC track beam (unit: mm): (a) elevation view of TB01; (b) plane view of TB01; (c) static deflection test sections (A-A/B-B/F-F/G-G); (d) static deflection and dynamic strain test sections (C-C and E-E); (e) static strain test section (D-D); (f) dynamic deflection and acceleration test section (D-D); (g) dynamic strain test section (D-D)

Ambient vibration tests were conducted to generate free vibration and investigate the natural frequencies, mode shapes, and damping ratio of each track beam. In order to evaluate the safety and comfort of the train when passing through the PC track beam, train load tests were conducted under empty loading and heavy loading conditions in the following scenarios:

(1) One monorail train passes the track beams of straight section at speeds of 5, 10, 20, 30, 40, 50, and 60 km/h, respectively.
(2) One monorail train passes the track beams of the curve section at speeds of 5, 10, 20, 30, and 40 km/h, respectively.
(3) One monorail train brakes on the track beams of the straight section at a driving speed of 20, 30, 40 km/h, respectively.
(4) One monorail train brakes on the track beam of the curve section at a driving speed of 20 and 30 km/h, respectively.

In each of the above tests, dynamic responses such as strain, deflection, acceleration and displacement amplitude of critical sections were measured. The locations of the critical sections are marked in Fig. 1(a), and their section information is shown in Figs. 1(c) to (g). The dynamic amplification factors of each PC track beam were calculated. The torsional angels were calculated to evaluate the torsional resistance of the PC track beams in the curve section.

3.2 Instrumentation

Displacement and strain were measured at several critical sections in the static test. As shown in Fig. 1(a), the measurement points for the vertical displacement were distributed on the sections A-A to G-G. The bottom of each section was connected to a dial gauge (model: WBD-50) (Shi *et al.* 2016) using steel wires. The specific test positions are shown in Figs. 1(c) and (d). The measurement points for the strains were arranged on the most unfavorable section of the track beam. Fig. 1(e) shows that 12 strain gauges were installed in the D-D section of each PC track beam. A two-part epoxy was used to mount the strain gauges on the surface of the beam. In the ambient vibration tests, six vibration sensors were employed in each beam to measure the self-vibration characteristics, as shown in Fig. 1(a).

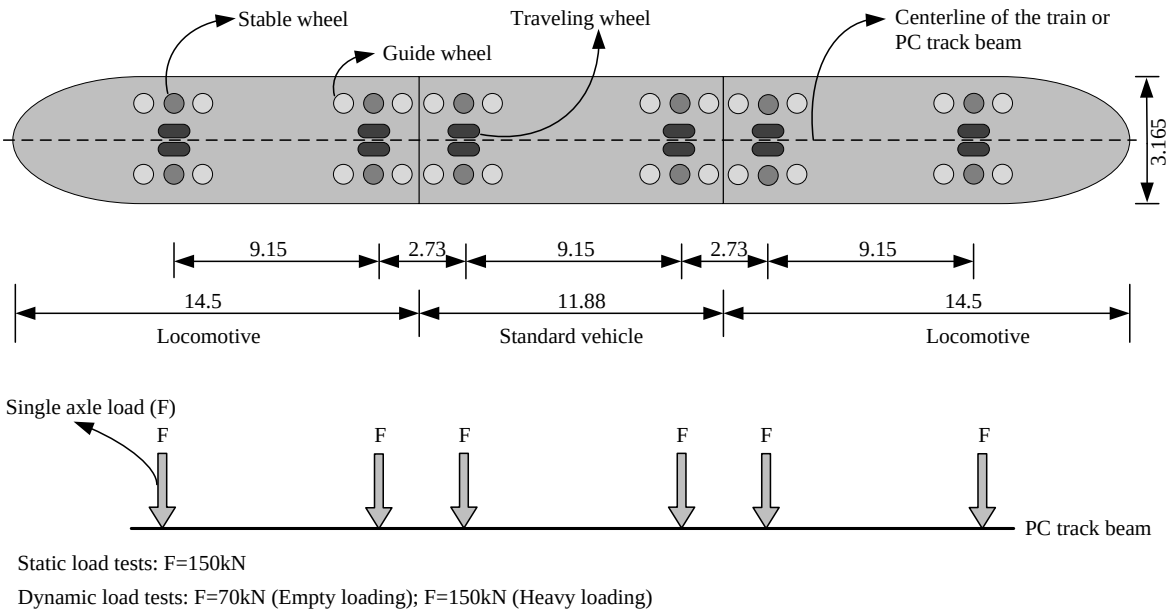

Fig. 2 Load distribution of the monorail train (unit: m)

For the dynamic load tests, more sections were monitored using sensors, including the D-D section, the C-C section, and E-E section. As shown in Figs. 1(g) and (d), four strain gauges were used in each section. As shown in Fig. 1(f), three sets of dial gauge were used to measure the displacement of the D-D section. Two sets of the dial gauge were connected to the bottom of the track beam to test the vertical displacement, and the other set of the dial gauge was connected to the side of the track beam to measure the lateral displacement. The acceleration sensors were bolted to the track beam, and the number and arrangement are the same as the displacement sensors. Two UCAM-70A (Wang *et al*. 2011) and two DEWE-BOOK16 (Deng *et al*. 2007) data acquisition systems were used to collect the static and dynamic load test data, respectively. Considering the difference in the natural frequency of each track beam, the sampling theorem (Jerri 2005) and the existing Chinese code (DBJ/T 2014) requirements, the sampling frequency was set to 25 Hz to 40 Hz in the data acquisition system.

3.3 Monorail trains

The monorail train used for static and dynamic load tests consisted of two head vehicles at the two ends and one standard vehicle in between, as shown in Fig. 2. Since the PC track beams were simply supported, applying load to the mid-span led to the most unfavorable internal loading. In the static load tests, the maximum load (single axle load (F) = 150 kN) of the train was used as the test load. The load was arranged according to the influence line of the moment at the mid-span of the track beam, resulting in the maximum positive moment (M_{max}) in the section. Taking TB01 as an example, the most unfavorable arrangement of train loads is shown in Fig. 3. The moments for all the track beams are shown in Table 2. In the dynamic load test, both the empty loading and heavy loading conditions of the train are included, as shown in Fig. 2.

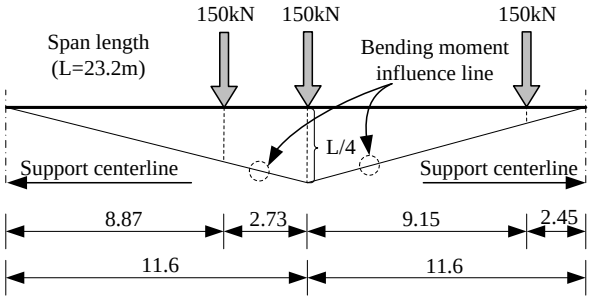

Fig. 3 The most unfavorable arrangement of train loads on TB01 (unit: m)

Table 2 Test bending moments for static load tests

Designation	Span length (unit: m)	M_{max} (unit: kN·m)
TB01	23.2	1719
TB02	19.2	1296
TB03	15.9	993
TB04	17.235	1095

4. Experimental results and discussions

4.1 Static strain

Each of the track beams was fully pre-stressed. Under the design loads, the behaves of the beam within the linear elastic range. To fully understand the static properties of the PC track beam, the finite element software Midas/Civil (Sun *et al*. 2018) was used to analyze the PC track beam. Under the same load condition, the deflection and cross section strain of each PC track beam were analyzed and compared with the test results. Figure 4 shows the test and simulation results of the strains at the D-D section of each

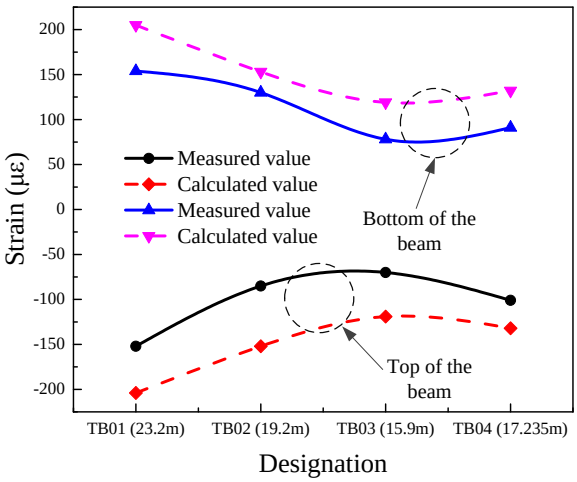

Fig. 4 Strain values at D-D section

track beam under the static loading. The strain of the cross section increases with the span length (L). The absolute values of the measured strain are less than the simulation results, likely because the Young's modulus of concrete adopted in the simulation was lower than that of the beams.

4.2 Static deflection

Fig. 5 shows the test and simulation results of the mid-span deflection of each beam under static loading. With the reduction of the span length, the deflection of the beam shows a decreasing trend at one-quarter (C-C section), one-half (D-D section), and three-quarter (E-E section) of the beam. Similar to the static strain, the vertical deflection of each track beam is less than the simulation results, indicating that the actual vertical stiffness of the track beam

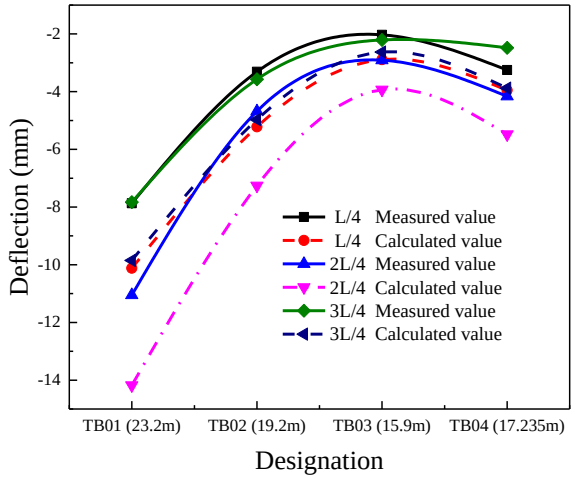

Fig. 5 Static deflection of each track beam

Table 3 Structural adjustment factors

SDF	TB01	B02	TB03	TB04
Strain	0.73–0.75	0.56–0.85	0.59–0.66	0.79–0.77
Deflection	0.71–0.79	0.63–0.72	0.70–0.84	0.64–0.82

is greater than the design values. The structural adjustment factor (SDF) is introduced to evaluate the load-bearing capacity of the track beams. The SDF is the ratio of the measured values to the theoretical values of the deflection and strain, as shown in Table 3. Compared with the "Code for rating existing railway bridges" (Railway Transport [2004] No. 120), the structural adjustment factors of the deflection and strain of each track beam under the static loading are within a reasonable range.

4.3 Vibration characteristics

Based on the acceleration measured in the ambient vibration tests (Kudu *et al*. 2014, Toydemir *et al*. 2017), the natural frequencies of the track beam can be determined by Fast Fourier Transform (FFT) analysis and peak detection method (Androus *et al*. 2017). The vibration mode analysis was performed using the modal parameter identification method (Kashani and Nobari 2012). Taking the TB01 track beam as an example, the first mode shape in both vertical and lateral direction can be obtained based on the vertical and lateral acceleration measured in the ambient vibration tests, as shown in Figs. 6(a) and (b).

As shown in Fig. 7, in the first vibration mode, the frequency (F) of the TB01 PC track beam in the vertical direction is 5.82 Hz, and the frequency in the lateral

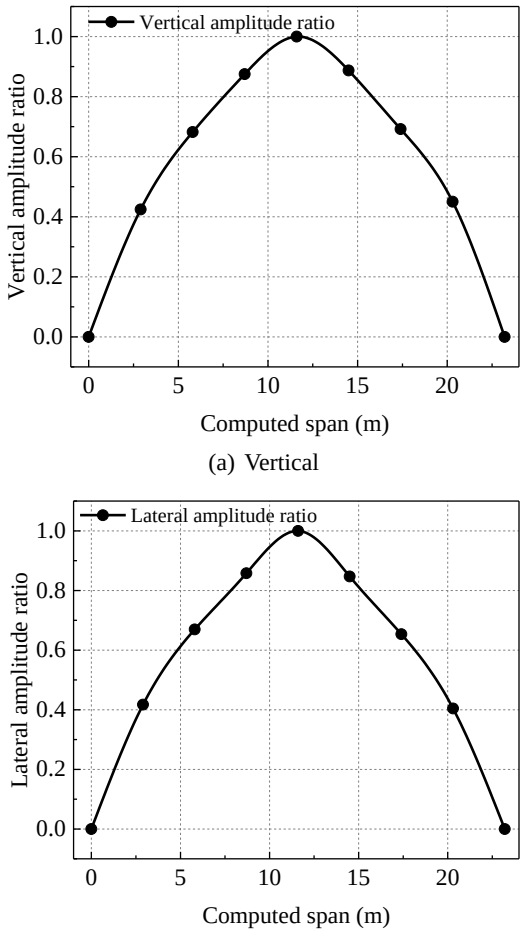

Fig. 6 First mode shape of the TB01

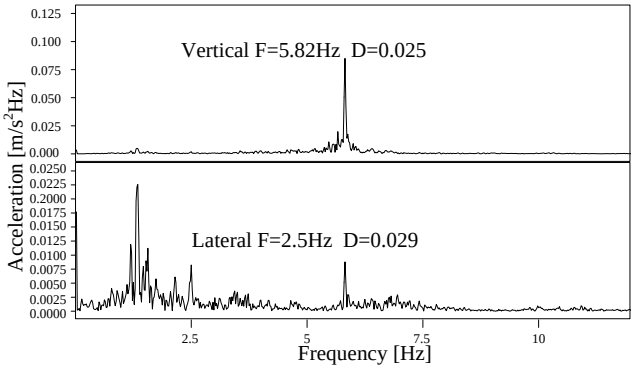

Fig. 7 Measured natural frequencies of the TB01

Table 4 Natural frequencies and damping ratio

Designation	First vibration mode	Measured frequency (Hz)	Calculated frequency (Hz)	Damping ratio
TB01	Vertical	5.82	5.01	0.025
	Lateral	2.50	2.00	0.029
TB02	Vertical	8.13	7.27	0.041
	Lateral	5.90	5.94	0.044
TB03	Vertical	10.79	10.38	0.033
	Lateral	7.15	7.80	0.029
TB04	Vertical	5.02	4.42	0.038
	Lateral	2.91	3.11	0.035

direction is 2.5 Hz. In addition, the damping ratio (D) of the track beam is calculated by the half-power spectral bandwidth method. For example, TB01 has a damping ratio of 0.025 in the vertical direction and 0.029 in the lateral direction.

The natural frequencies and damping ratio of each track beam in the first vibration mode are summarized in Table 4. Comparing the measured and calculated results, it is found that the measured value of the lateral natural frequencies are basically consistent with the calculated values, which shows a good lateral stiffness of each PC track beam. In addition, the measured vertical natural frequencies of all the track beams are higher than the calculated values, indicating that the actual vertical stiffness of the track beam is greater than the theoretical stiffness. The damping ratio of the track beam is small (between 0.025 and 0.044) and in reasonable agreement with the actual situation.

4.4 Dynamic deflection

Figs. 8(a) to (c) show the vertical maximum dynamic deflections of the mid-span (D-D section) of each track beam under dynamic load. With the increase of the train speed, the dynamic deflection of each track beam in the straight section, transition curve section and round section is stable, but the dynamic vertical deflections of the TB01 track beam are significantly larger than that of other track beams. Although the span length of the TB04 track beam is smaller than that of the TB02 track beam, the vertical dynamic deflection of the TB04 track beam is slightly larger. Therefore, it can be concluded that the train load and the span length of the track beam are the two main factors affecting the vertical deflection. The train speed has little effect on the vertical dynamic deflection of the PC track beam. When the span length of the PC track beam is approached, there will be greater vertical deflection of the smaller radius of curvature, which may be due to its more pronounced bending-torsion coupling effect.

Figs. 9(a) to (c) show the lateral maximum dynamic deflections of the mid-span of each PC track beam under dynamic loading. As can be seen from Fig. 9(a), under empty loading conditions, the train speed has little effect on the lateral dynamic deflection of TB01 in the straight section. However, under heavy loading conditions, the train speed has a great influence on the lateral dynamic deflection, especially after the train speed reaches 40 km/h, the lateral dynamic deflection increases rapidly. Moreover, when the train speed is less than 40 km/h, the lateral dynamic deflection of the TB01 track beam under heavy loading is smaller than that of under empty loading. This may be due to a relatively large load suppresses the lateral vibration of the straight track beam. Fig. 9(b) shows that the train speed has a significant impact on the lateral dynamic deflection of the TB02 and TB03 in the curve section. After the train speed reaches 20 km/h, the lateral dynamic deflection of the track beam under heavy loading suddenly

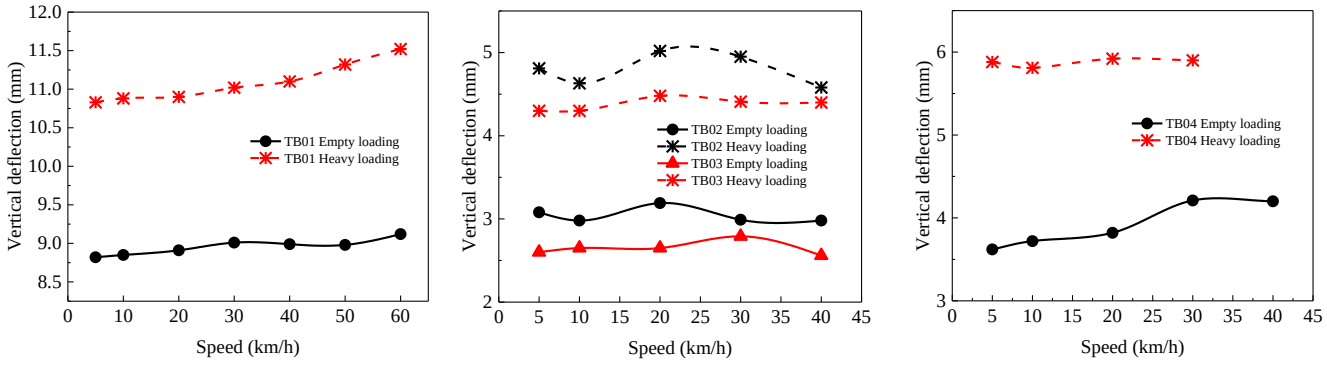

Fig. 8 Vertical dynamic deflection of monorail track beams

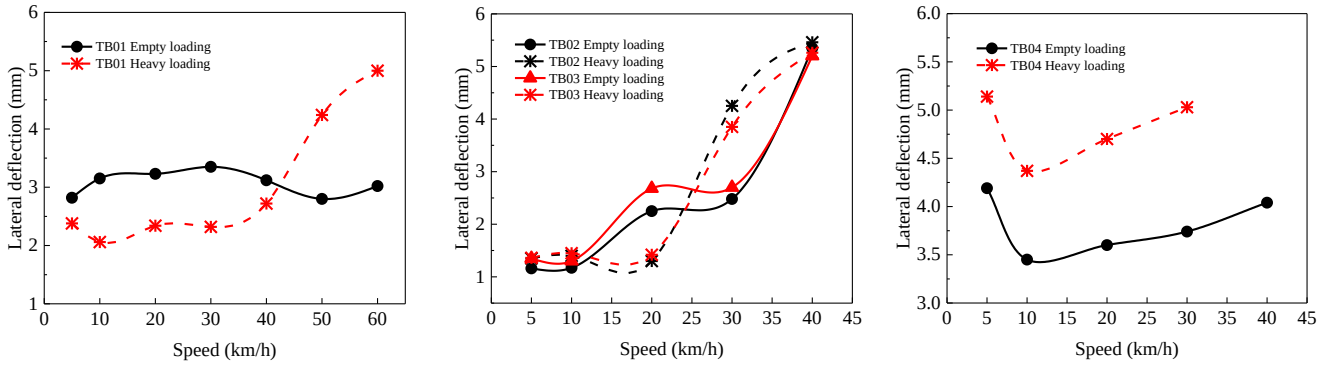

(a) Straight section (b) Transition curve section (c) Round curve section

Fig. 9 Lateral dynamic deflection of monorail track beams

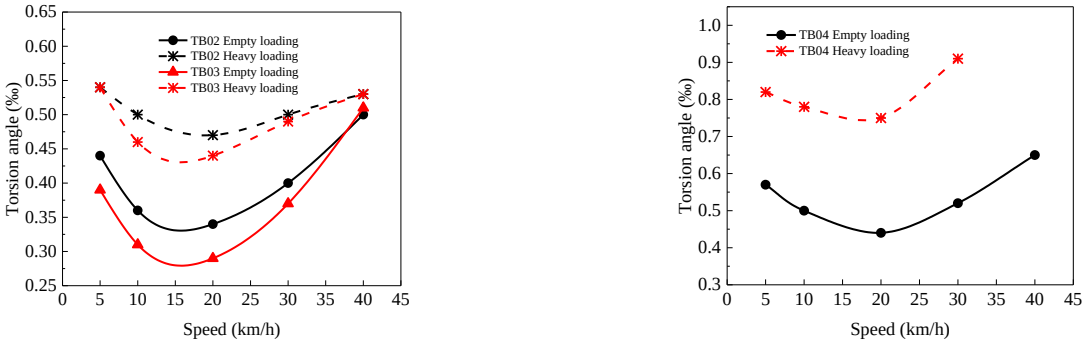

(a) D-D section (b) D-D section

Fig. 10 Measured torsion angle of each track beam in the curve section

increases. Under empty loading, the phenomenon is also observed after the train speed reaches 30 km/h. For TB04, the maximum lateral dynamic deflection first decreases and then increases. When the speed of the train is 10 km/h, the lateral dynamic deflection of the track beam achieves the minimum value, as shown in Fig. 9(c), and which may be related to the centrifugal force and train speed. Therefore, the radius of curvature of the track beam, the train speed and load are all important factors for lateral dynamic deflection.

4.5 Torsion analysis

Figs. 10(a) and (b) show the maximum torsional angle of the D-D section of each track beam in the curved section under empty loading and heavy loading conditions. As the train speed is increased from 5 to 40 km/h, the torsion angles of the TB02, TB03 and TB04 at the D-D section first decrease and then increases. At the train speed of 20 km/h, the torsion angle is the smallest. As shown in Fig. 10(b), the maximum torsion angle of the track beam in the round curve section is significantly greater than that of in the transition curve section. This may be due to the fact that TB04 has a smaller radius, so the track beam undergoes a larges torsional load.

The detailed results of the maximum torsion angles for each track beam are summarized in Table 5. The maximum torsion angle of the track beam occurs under heavy loading condition. The maximum torsion angle at the D-D section of TB02 and TB03 is 0.54‰, and the maximum torsion angle at the D-D section of the TB04 track beam is 0.91‰. Overall, the torsional angles of the various track beams are very small, indicating that each beam body has good torsional resistance.

Table 5 Measured maximum torsion angle of track beams

Designation	Empty loading	Heavy loading
	Torsion angle (D-D section)	Torsion angle (D-D section)
TB02	0.51‰	0.54‰
TB03	0.50‰	0.54‰
TB04	0.65‰	0.91‰

4.6 Displacement amplitude

The vertical and lateral displacement amplitudes at the D-D section were measured when the train moves on the track beam. As shown in Figs. 11(a) to (c), the vertical displacement amplitudes of each track beam increase with the train speed. The maximum vertical amplitude of the track beam is 1.71 mm in the straight section, and is 1.37 mm within the curve section. Regardless of the empty/heavy loading, the vertical displacement amplitudes of TB02 are greater than that of TB03, as shown in Fig. 11(b). This may be caused by the different span lengths.

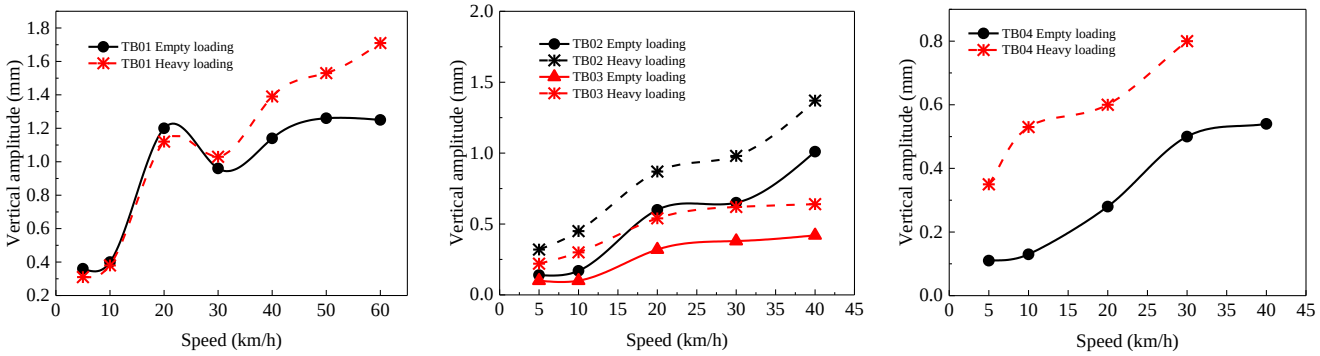

(a) Straight section (b) Transition curve section (c) Round curve section

Fig. 11 Measured maximum vertical amplitudes of each track beam at D-D section

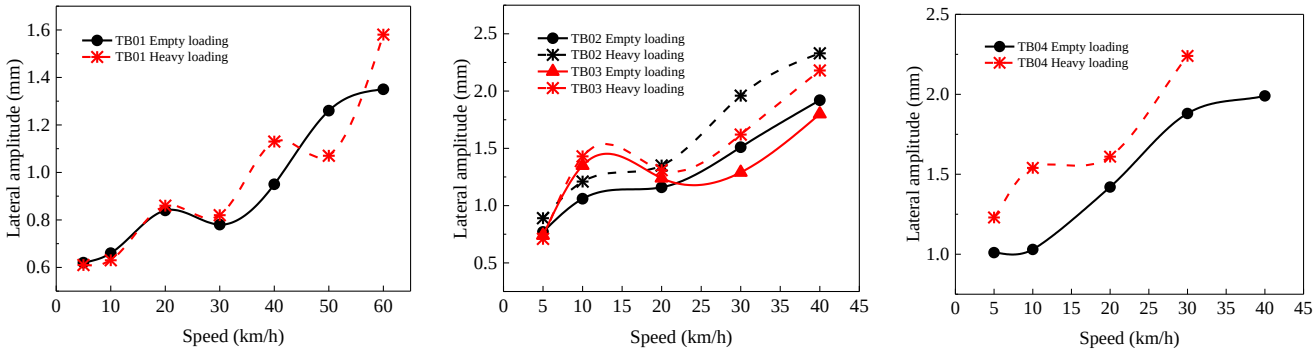

(a) Straight section (b) Transition curve section (c) Round curve section

Fig. 12 Measured maximum lateral amplitudes of each track beam at D-D section

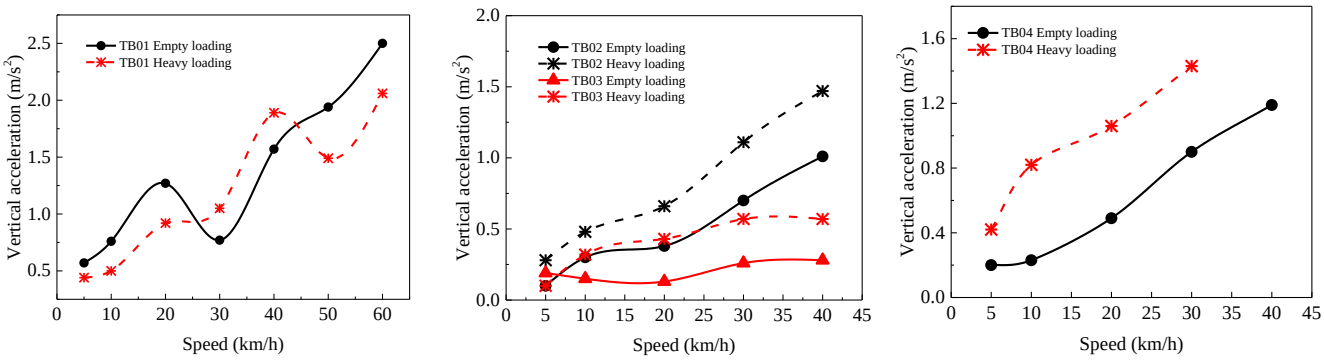

(a) Straight section (b) Transition curve section (c) Round curve section

Fig. 13 Measured vertical peak accelerations of each track beam at D-D section

In the lateral direction, the displacement amplitudes of each track beam have a significant fluctuation. The amplitude of the lateral displacement of the track beam under heavy loading is greater than that under empty loading. As the train speed is increased from 5 to 60 km/h, the lateral displacement amplitude of the track beam in the straight section approximately linearly increases, as shown in Fig. 12(a). The lateral displacement amplitudes of the track beams in the transition curve section and round curve section are generally larger than that of in the straight section, as shown in Figs. 12(a) and (b). The maximum lateral displacement amplitude of the track beam is 1.58 mm in the straight section, and is 2.33 mm within the curve section. Therefore, the lateral vibration of the track beam in the curve section may be more pronounced.

4.7 Acceleration

Figs. 13(a) to (c) show the vertical peak accelerations measured at the D-D section of each track beam under the action of a moving train. Overall, the vertical peak accelerations of each track beam increase with the train speed. In the straight section (TB01), as the speed is increased from 5 to 60 km/h, the vertical peak accelerations

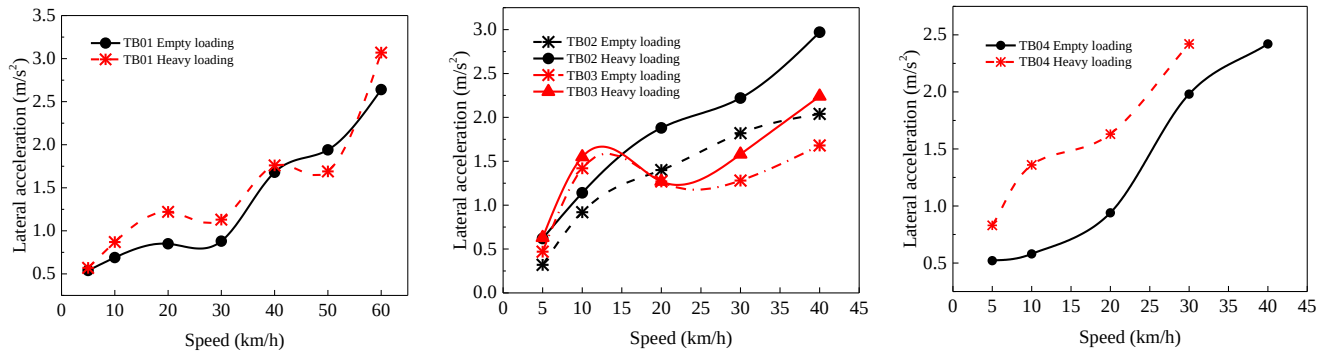

(a) Straight section (b) Transition curve section (c) Round curve section

Fig. 14 Measured lateral peak accelerations of each track beam at D-D section

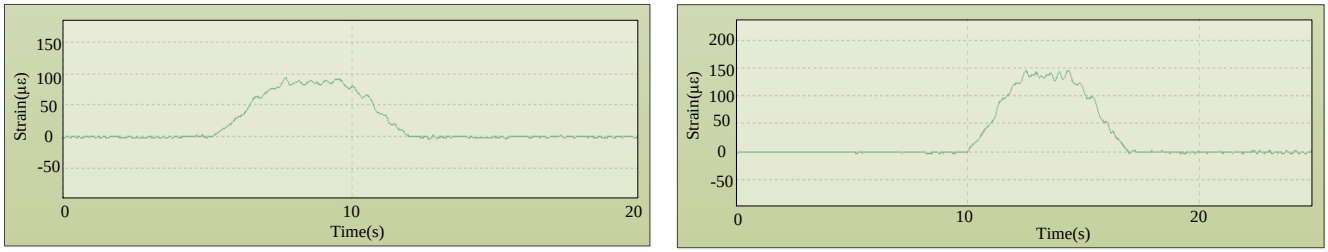

(a) Empty loading (b) Heavy loading

Fig. 15 The time-history of the dynamic strain on the tension side of D-D section of TB01

are increased from about 0.44 to 2.5 m/s^2. In the curve section, as the speed is increased from 5 to 40 km/h, the vertical peak accelerations are increased from about 0.1 to 1.47 m/s^2. Under the same speed and loading conditions, the vertical peak accelerations in the straight section are usually large that of in the curve section.

In the lateral direction, the lateral peak acceleration increases approximately linearly with the train speed, as shown in Figs. 14(a) to (c). Therefore, the maximum lateral peak acceleration of each track beam occurs when the train speed reaches a maximum. Under the same speed and load conditions, the lateral peak acceleration of the track beam in the curve section is obviously larger than that of in the straight section. Specifically, under heavy loading conditions, the lateral peak acceleration of the track beam in the straight section reaches approximately 3 m/s^2 at a train speed of 60 km/h. At the same time, when the train speed is 40 km/h, the lateral peak acceleration of the TB02 track beam reaches a maximum value of about 3 m/s^2.

Compared with the "Code for rating existing railway bridges" (Railway Transport [2004] No. 120), it can be found that many peak accelerations are beyond the allowable range. Therefore, during the actual train operation, the radius of curvature of the track beam, the speed and load of the train should be properly controlled, and the optimal design of the structure can also be considered.

4.8 Dynamic amplification factor

The amplification factor (Gou *et al*. 2018c) reflects the dynamic effect of the moving train on the strains at critical locations of the track beam. A dynamic amplification factor (μ) is introduced for the dynamic effects on the beam

$$\mu = \frac{2\varepsilon_{\max}}{\varepsilon_{\max} + \varepsilon_{\min}} \tag{1}$$

where $\varepsilon_{\max}$ and $\varepsilon_{\min}$ are the measured maximum and minimum values of strain respectively when the train moves on the track beam.

Figs. 15(a) and (b) respectively show the time-history of the dynamic strain on the tension side of D-D section of TB01 when the train is running at 30 km/h under empty loading and heavy loading conditions. Due to the dynamic components, the time-history under heavy loading and empty loading is not a smooth curve.

Figs. 16(a) to (c) describe the variation of the dynamic amplification factor with the train speed at the D-D section (Measuring point 1) of each track beam. As shown in Figs. 16(a) and (c), the peak dynamic amplification factors of the track beam in the straight section and the round curve section appear when the train speed is 30 km/h. For the transition section, the peak dynamic amplification factors of the track beam appear at the train speed of 40 km/h, as shown in Fig. 16(b). The dynamic amplification factors of the track beam in the curve section are larger than that in the straight section, due to a combination of various factors such as the radius of curvature and the span length. An interesting phenomenon is that the dynamic amplification factors under empty loading conditions are larger than that of under heavy loading, which indicates that the heavy loading conditions of the train may have an inhibitory effect on the dynamic amplification factors of the track beam.

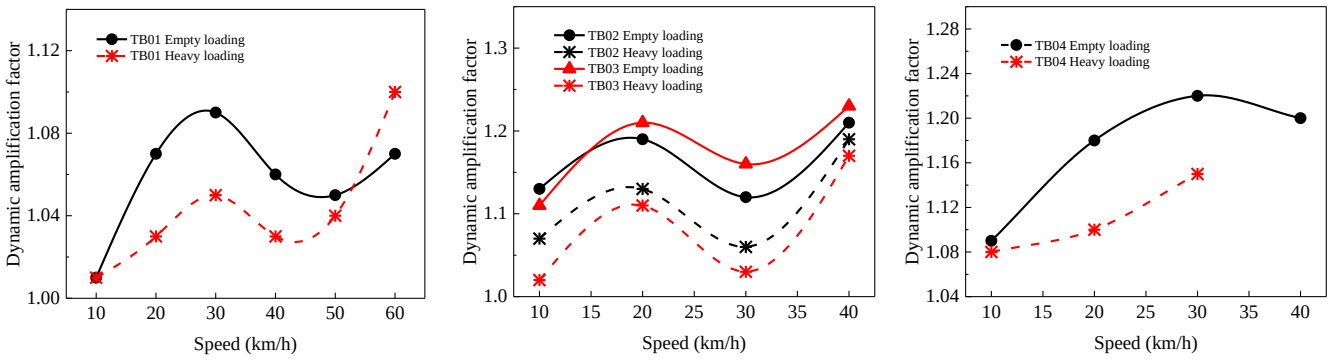

(a) Straight section (b) Transition curve section (c) Round curve section

Fig. 16 Strain dynamic amplification factors at the tension side of D-D section of each PC monorail track beam

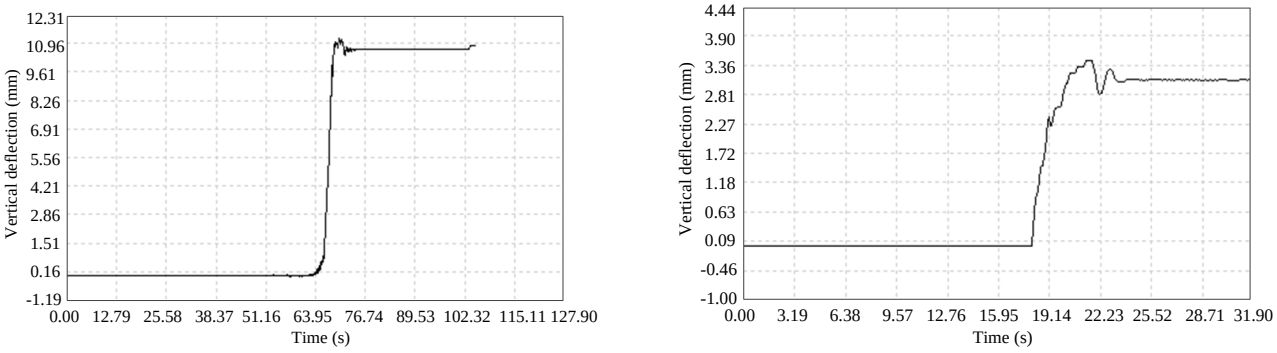

(a) (b)

Fig. 17 Vertical deflection at the mid-span of TB01 and TB03 when the monorail train is braking at 30 km/h under heavy loading conditions: (a) TB01; (b) TB03

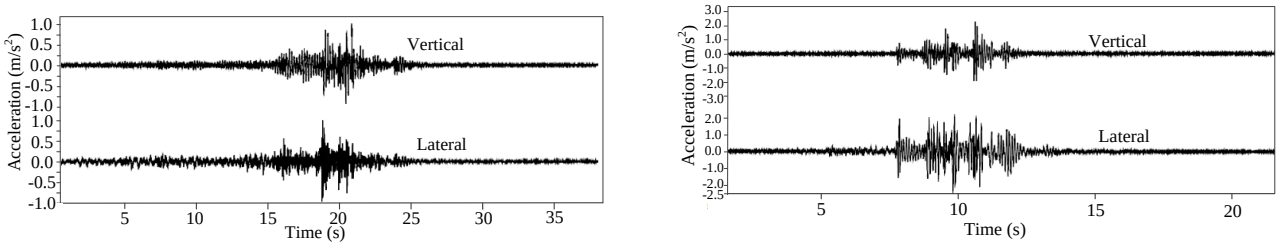

(a) (b)

Fig. 18 Vertical and lateral accelerations of the track beam when the train is braked at a speed of 30 km/h under heavy loading conditions: (a) TB01; (b) TB03

4.9 Effect of train braking

In the train brake test, the dynamic responses of the track beam are analyzed when sudden brick is applied to a train. For the straight sections, the train speeds are 20, 30 and 40 km/h, respectively, while for the curve sections, the train speeds are 20 and 30 km/h, respectively. Figs. 17(a) and (b) show the measured vertical deflections of TB01 and TB03, respectively, when the monorail train is braked at 30 km/h under heavy loading. The mid-span vertical deflection of TB01 is significantly greater than that of TB03. This difference may be mainly affected by the span length of track beam.

Figs. 18(a) and (b) show the acceleration of TB01 and TB03 in the vertical and lateral directions, respectively, when the train is braked at a speed of 30 km/h. If the train suddenly brakes, whether in the vertical or lateral direction, the acceleration of TB03 is slightly larger than that of TB01. The reason may be mainly due to the difference in radius of curvature of the beam body. The braking effect is the greatest in the areas near the train.

5. Finite element analysis

Finite element analysis has been performed to analyze the dynamic responses (Turker *et al.* 2007, Votsis *et al.*

2017). In this study, finite element models of the track beam and trains were established using the software Midas/Civil, considering the track irregularity and interaction between the train and the track beams.

5.1 Bridge model

In order to fully excite the vibration of vehicles and bridges, the PC simply supported beam bridge is set to 5 spans. The length of each span is 23.2 m; the height of piers is 11 m. The bridges are considered as an assembly of beam elements with six DOFs at each node. The finite element model of the bridge is shown in Fig. 19. The material properties of the bridge are shown in Table 6. The consistent mass system and Rayleigh damping are used to establish the mass and damping matrices of the bridge model. The equation for forced vibration of a bridge under a moving monorail train is given by

$$\mathbf{M_b}\ddot{\mathbf{u}}_\mathbf{b} + \mathbf{C_b}\dot{\mathbf{u}}_\mathbf{b} + \mathbf{K_b}\mathbf{u_b} = \mathbf{P_b} \tag{2}$$

where, $\ddot{\mathbf{u}}_\mathrm{b}$, $\dot{\mathbf{u}}_\mathrm{b}$ and $\mathbf{u}_\mathrm{b}$ respectively represent the nodal acceleration, velocity and displacement vectors of the bridge. $\mathbf{M_b}$, $\mathbf{C_b}$ and $\mathbf{K_b}$ represent the mass, damping and stiffness matrices of the bridge, respectively. $\mathbf{P_b}$ is the external force vector due to a moving train.

5.2 Monorail train model

A straddle monorail vehicle consists of body, bogies, traveling wheels, guide wheels and stable wheels, suspension system and shock absorber. The body is connected to the front and rear bogies by secondary suspension systems. Due to the multi-directional elasticity of rubber tires, there is no suspension between the bogies and wheels. The following assumptions are proposed in the modeling of monorail train:

(1) Both the body and the bogie are rigid, and the nonlinear characteristics of the suspension system are not considered.
(2) The train passes the track beams at constant speed and the wheels of a train remain in contact with the surface of the track beam.
(3) The body, bogies and wheelsets of the train have negligible vibrations, and the interactions between vehicles are ignored.
(4) The effect of vertical loads on the stiffness characteristics of the running wheels is not considered.

In the dynamic analysis, each monorail vehicle is idealized as a model with 18 DOFs as shown in Figs. 20 and 21. The symbols X, Y and Z indicate the lateral, longitudinal, and vertical directions, respectively; ψ, φ and θ denote the shaking, rolling and nodding displacement, respectively.

The equation of motion for a travelling monorail train on a bridge can be expressed as

$$\mathbf{M_v}\ddot{\mathbf{u}}_\mathbf{v} + \mathbf{C_v}\dot{\mathbf{u}}_\mathbf{v} + \mathbf{K_v}\mathbf{u_v} = \mathbf{P_v} \tag{3}$$

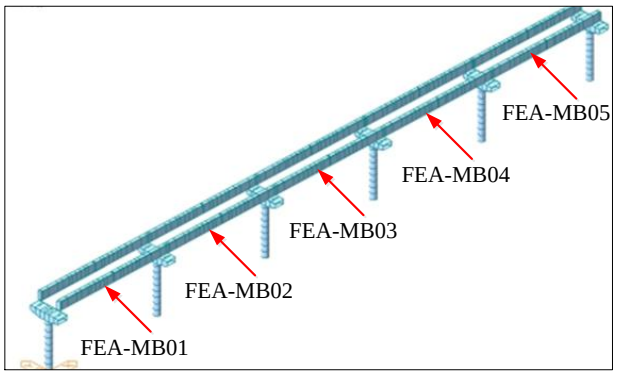

Fig. 19 Finite element model

Table 6 Material properties of the bridge

Components	Materials	Young's modulus (GPa)	Poisson ratio	Density (kg/m^3)
Beam body	C60 concrete	36.5	0.2	2500
Pier and Cover beam	Composite materials	206	0.3	7700

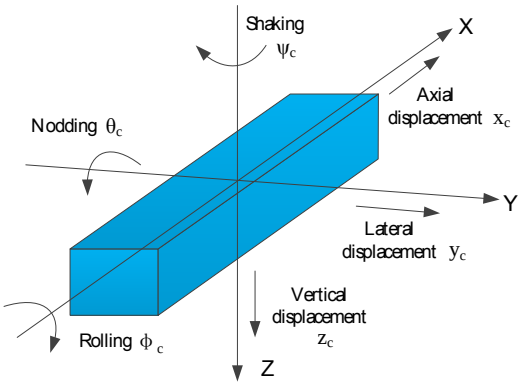

Fig. 20 Multiple DOF of the vehicle body

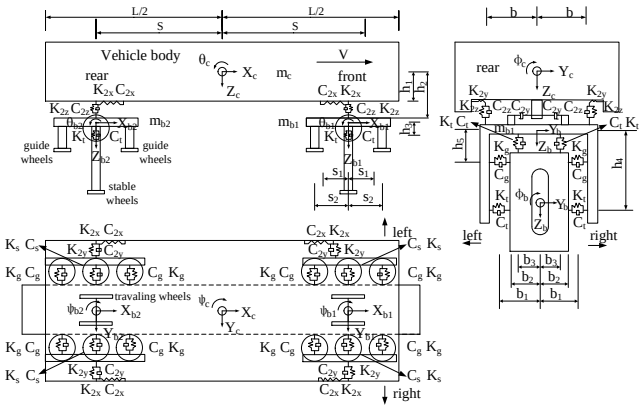

Fig. 21 Monorail train model with 18 DOFs

where, $\ddot{\mathbf{u}}_v$, $\dot{\mathbf{u}}_v$ and $\mathbf{u}_v$ respectively, represent the acceleration, velocity and displacement vectors of the train. $\mathbf{M}_v$, $\mathbf{C}_v$ and $\mathbf{K}_v$ represent the mass, damping and stiffness matrices of the train, respectively. $\mathbf{P}_v$ is the interaction force vector applied on the train. Rayleigh damping is adopted to form the damping matrix.

5.3 Track irregularity

Track irregularity is an important source of excitation for the vehicle-bridge coupled vibration of a monorail system (Wang *et al*. 2018). In the previous studies, power spectral density function was used to describe the irregularity of orbital surface. (Lee *et al*. 2005) carried out a field-test on the surface random irregularity of monorail steel track beam, and gave the formula as follows

$$S(\Omega)=\frac{\alpha}{\Omega^n+\beta^n} \tag{4}$$

where S denotes the spectral density functions of track irregularity; Ω denotes the spatial frequency (cycle/m); α, β and n are the parameters that represent the shape of the spectral density function. The values of the parameters α, β and n are shown in Table 7.

Since the track irregularity random function is similar to the stationary Gauss stochastic process, the triangular series superposition method is used to form the surface irregularity random samples. The equation of the triangular series superposition method can be expressed as

$$y(x)=\sum_{i=1}^{n}\sqrt{2S(\Omega_i)\Delta\Omega}\cdot\cos(2\pi\Omega_i x+\varphi_i) \tag{5}$$

where $y(x)$ is the surface irregularity random sample, x, indicate the location in which the track irregularity is generated; $\Delta\Omega = (\Omega_n - \Omega_1)/n$, which represents the bandwidth of the frequency interval, where Ω_n, Ω_1, represent the upper and lower limits of the frequency being considered, respectively. $\Omega_i = \Omega_1 + (i - 0.5)\Delta\Omega$, indicates frequency component; $S(\Omega_i)$ is the power spectral density function of the surface roughness of a given track beam, as shown in Eq. (4); and φ_i represents a random phase angle which is distributed uniformly between 0 to 2π. A sample of the track irregularity of the track beam under traveling wheel is presented in Fig. 22.

5.4 Monorail train-bridge interaction

The vehicle system and the bridge system are coupled through the wheel-track contact relationship. The geometric compatibility conditions at the contact point between the vehicle and the bridge can be written as

Table 7 Parameters of track irregularity

Location	Parameters
Surface of traveling wheel	α = 0.0005, β = 0.35, n = 3.00
Surface of guild wheel	α = 0.0006, β = 0.50, n = 2.80
Surface of stable wheel	α = 0.0006, β = 0.50, n = 2.60

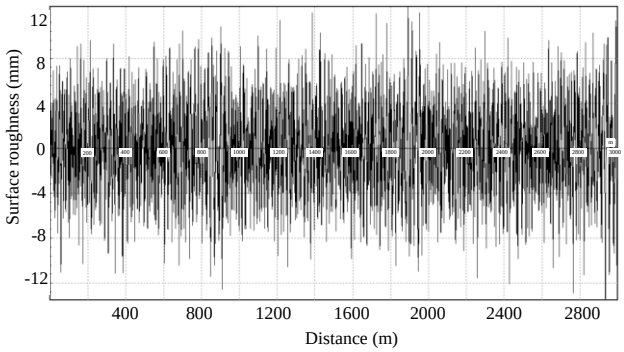

Fig. 22 Sample track irregularity of the track beam at the traveling wheel

$$\mathbf{U}_v^i=\mathbf{U}_b^i+y_s \tag{6}$$

The static equilibrium conditions for the wheel rail interaction force at the contact point can be expressed as

$$\mathbf{P}_{bv}^i=\mathbf{P}_{vb}^i \tag{7}$$

where i denotes the i_{th} contact point; y_s denotes the displacement vector caused by the track irregularity; $\mathbf{P}_{bv}^i$ denotes the force of the train acting on the bridge; $\mathbf{P}_{vb}^i$ denotes the force of the bridge acting on the train.

Eqs. (2) and (3) of the train and the bridge can be integrated through Eqs. (6) and (7). The train-bridge coupled motion equation for a monorail system can be described as

$$\begin{bmatrix}\mathbf{M}_b & 0\\ 0 & \mathbf{M}_v\end{bmatrix}\begin{bmatrix}\ddot{\mathbf{u}}_b\\ \ddot{\mathbf{u}}_v\end{bmatrix}+\begin{bmatrix}\mathbf{C}_b & \mathbf{C}_{bv}\\ \mathbf{C}_{vb} & \mathbf{C}_v\end{bmatrix}\begin{bmatrix}\dot{\mathbf{u}}_b\\ \dot{\mathbf{u}}_v\end{bmatrix}+\begin{bmatrix}\mathbf{K}_b & \mathbf{K}_{bv}\\ \mathbf{K}_{vb} & \mathbf{K}_v\end{bmatrix}\begin{bmatrix}\mathbf{u}_b\\ \mathbf{u}_v\end{bmatrix}=\begin{bmatrix}\mathbf{P}_b\\ \mathbf{P}_v\end{bmatrix} \tag{8}$$

where **M**, **C** and **K** indicate the mass, damping and stiffness matrices, respectively; and **P** is the force vector. Subscripts b, v, bv (or vb) denote the bridge, vehicle (train), and vehicle-bridge interaction, respectively. The solution of the dynamic response of the train-bridge system is achieved by the self-compiled program in FORTRAN language. The motion equations of the train-bridge interaction are solved by the Newmark-β integral method (Guo and Xu 2001). The calculation parameters in the method, γ and β are 0.5 and 0.25, respectively. The time step (Δt) is set to 0.001 s.

6. Numerical results and discussion

6.1 Model validation

To validate the finite element model and investigate the coupled vibration of straddle monorail bridge-train, a self-programming program (SPP) based on FORTRAN (Wang *et al*. 2018) was developed. The bridge natural frequency calculated by SPP and MIDAS is shown in Table 8. The first few vibration modes of the bridge vibration are the longitudinal bending of the pier. The first-order natural frequency of the bridge in the lateral direction is 1.798 Hz,

Table 8 Free vibration characteristics of the bridge

Mode No.	Frequency (Hz)			Description of vibration mode
	Midas	SPP	Difference	
1	1.737	1.802	3.7%	The longitudinal bending of the pier
2	1.798	1.837	2.0%	Lateral bending of main beam
4	1.863	1.922	3.2%	The lateral bending of the pier
14	4.808	4.725	1.7%	Vertical bending of main beam

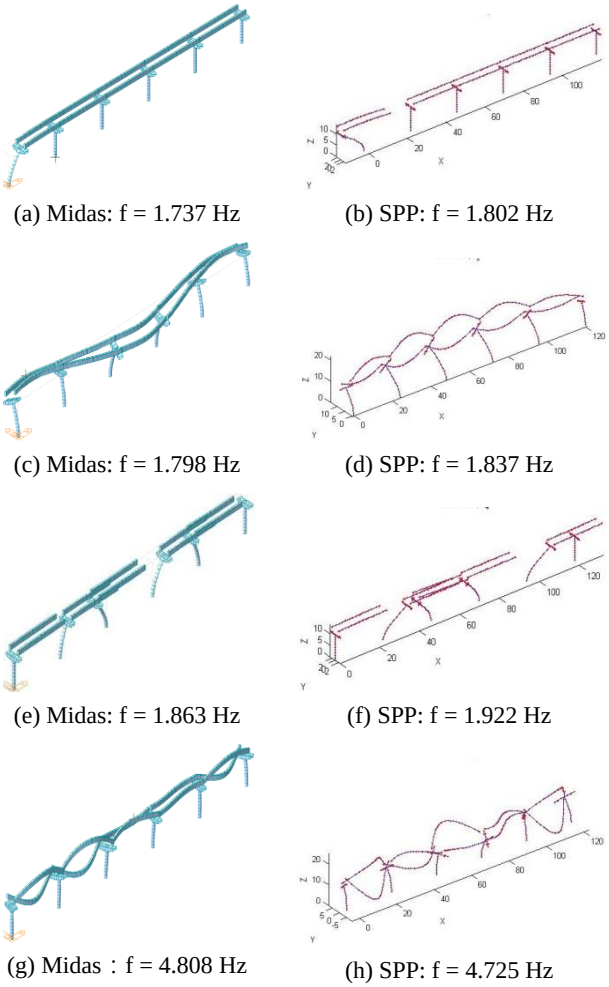

(a) Midas: f = 1.737 Hz (b) SPP: f = 1.802 Hz

(c) Midas: f = 1.798 Hz (d) SPP: f = 1.837 Hz

(e) Midas: f = 1.863 Hz (f) SPP: f = 1.922 Hz

(g) Midas：f = 4.808 Hz (h) SPP: f = 4.725 Hz

Fig. 23 Typical mode shape of the full bridge

and the vertical first-order natural frequency is 4.808 Hz. It can be seen from Table 7 that the discrepancy of the analysis results using the two methods is up to 3.7%, indicating that the analysis results are reasonable. The typical modes of the bridge calculated using the SPP and Midas are shown in Fig. 23.

6.2 Deflection and acceleration

Fig. 24 shows the vertical dynamic deflections at mid-span section of the FEA-MB03, FEA-MB04, and FEA

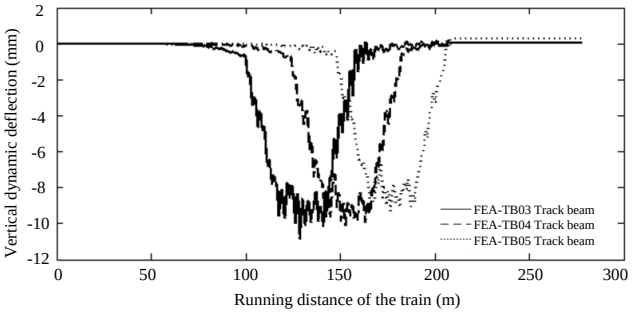

Fig. 24 Vertical dynamic deflection of each beam

MB05 under heavy loading at 50 km/h. There is no significant difference in the vertical dynamic deflection of the three track beams under the same condition.

Fig. 25(a) compares the in-situ test results from TB01 and finite element analysis results from FEA-MB03 and FEA-MB04. The measured value of the vertical dynamic deflection is slightly less than the calculated value, due to the fact that the actual stiffness of the track beam is greater. The maximum discrepancy is 7%. Fig. 25(b) compares the numerical and experimental values of the acceleration of the track beam at section D-D at various train speeds. The vertical deflection of the track beam approximately linearly increases in the train speed range of 10 to 50 km/h. The

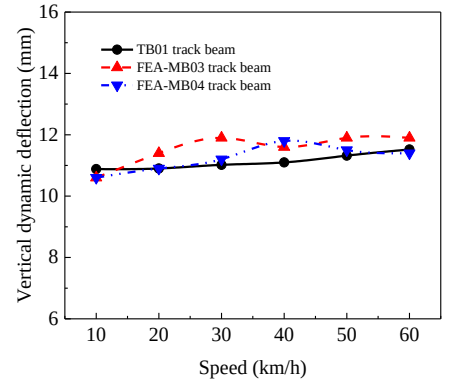

(a)

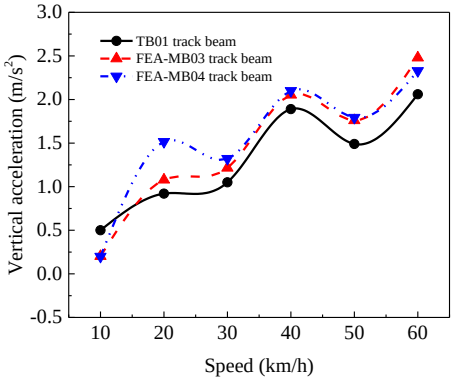

(b)

Fig. 25 Comparison of experimental and numerical results when one train travels through the bridge: (a) vertical dynamic deflection; (b) vertical dynamic acceleration

Table 9 Evaluation criteria of the comfort index

Grade	Comfort index	Description
Class 1	$N < 1$	Excellent
Class 2	$1 \le N < 2$	Good
Class 3	$2 \le N < 4$	Meet the requirement
Class 4	$4 \le N < 5$	Allow operation
Class 5	$N \ge 5$	Not allowed to run

Table 10 Frequency correction factor (UIC513)

Vertical vibration		Lateral vibration	
0.5~6.9 Hz	$F(f) = 0.325f^2$	0.5~6.4 Hz	$F(f) = 0.8f^2$
6.9~20.0 Hz	$F(f) = 400/f^2$	6.4~26.0 Hz	$F(f) = 650/f^2$
> 20.0 Hz	$F(f) = 1$	> 26.0 Hz	$F(f) = 1$

simulation results are in reasonable agreement with the test results, validating the finite element model.

7. Evaluation of riding comfort

Comfort and stability are key indicators for the riding comfort of a train, which comprehensively reflects the impact of the vehicle vibration on the comfort of passengers. The comfort index can be calculated as follows (ISO2631. 1985, UIC513. 1994)

$$N = 6\sqrt{(a_{XP95}^{W_d})^2 + (a_{YP95}^{W_d})^2 + (a_{ZP95}^{W_b})^2} \tag{10}$$

where N represents the comfort index; a represents the RMS value of the acceleration; W_d, W_b represent that the acceleration values are weighted according to frequency (see ISO 2631 standard); d and b represent the horizontal and vertical directions, respectively; X, Y, and Z respectively indicate the longitudinal, lateral, and vertical directions of the acceleration sensor; P indicates that the sensor is located on the floor of the train; 95 indicates that the acceleration is an effective value at a 95% confidence point. The grading of the comfort index is shown in Table 9.

Table 11 Evaluation criteria of stability index

Grade	Stability index	Description
Class 1	< 2.5	Excellent
Class 2	2.5~2.75	Good
Class 3	2.75~3.0	Qualified

The running stability of trains is evaluated using the Sperling index, which can be expressed as (Zhai 2015)

$$W = 7.08\sqrt[10]{\frac{A^3}{f}F(f)} \tag{11}$$

where A denotes the acceleration of vehicle (g), f is the vibration frequency (Hz), F (f) indicates frequency correction factor, as shown in Table 10.

The classification of the stability index is shown in Table 11 (UIC513). The comfort level and stability level of the test train should not be lower than level 2.

According to the test data, the evaluation results of the riding comfort of the train under various running conditions calculated by ISO2631 and UIC513 standards are shown in Fig. 26. Under empty loading conditions, when the train is running at a speed of 5 to 20 km/h, the comfort index value is less than 1 and judged as excellent. But when the speed of the train is greater than or equal to 30 km/h, the riding comfort of the train is reduced and both levels are rated as being good, as shown in Fig. 26(a). Under heavy loading conditions, most of the comfort levels of the train belonged to Class 2 and were described as good, as shown in Fig. 26(b). Overall, the comfort of the monorail train is good when the train is running on various track beams. In addition, for the lateral and longitudinal stability of monorail trains, the stability index value is less than 2.5, which indicates that the stability level of the train can be rated as Class 1 and described as excellent.

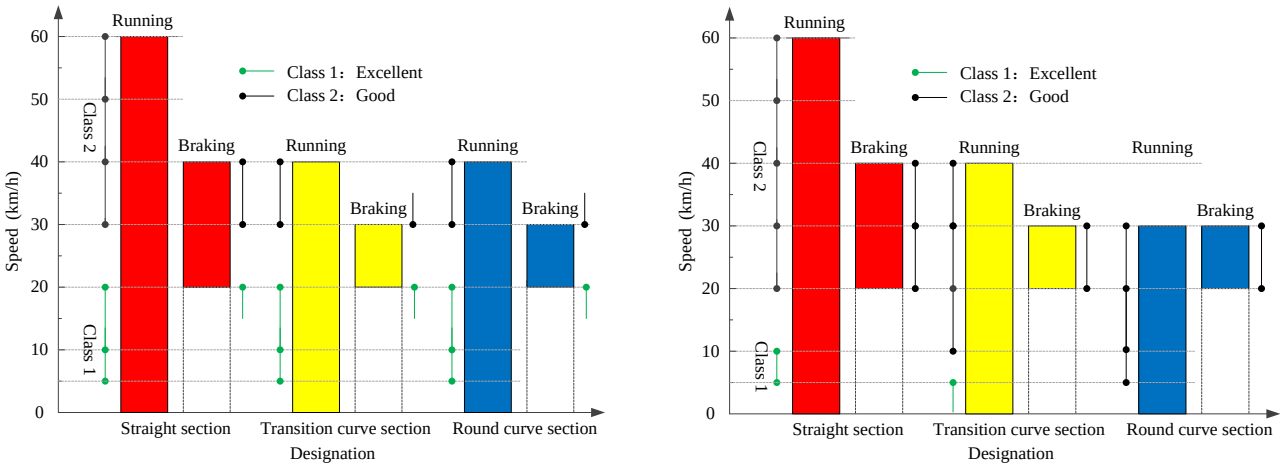

(a) Hmpty loading (b) Heavy loading

Fig 26 Evaluation of comfort when the train is running on the track beams in each section

8. Conclusions

Based on the experimental and numerical studies, the following conclusions can be drawn.

(1) In the static load tests, the measured deflection and strain of each PC track beam are less than the calculated values, showing sufficient strength and stiffness. The train speed has little effect on deflection and strain of the PC track beam. The train load and span length are two main influencing factors.
(2) With the increase of the train speed, the dynamic deflection of the track beam is stable in the straight section, transition curve section and round section. The train speed has a significant influence on the lateral dynamic deflection of the PC track beams, and the lateral dynamic deflection of the track beam in the curve section is more sensitive to the train's speed.
(3) The torsion effect of the track beam becomes more pronounced as the radius of curvature decreases and the train loads increases. The maximum torsion angle of the track beam under heavy loading is significantly greater than that under empty loading. The maximum torsion angle of the track beam in the round curve section is greater than that in the transition curve section.
(4) The amplitudes of the displacement and acceleration of each PC track beam increase approximately linearly with the train speed. The amplitude of vertical displacement under heavy loading is higher than that under empty loading. This phenomenon is more obvious in the curve section. The amplitude of the lateral displacement of the track beam in the curve section is greater than that in the straight section. The vertical peak acceleration of the straight-line segment is less than that in the curve section. The lateral peak acceleration of PC track beam in the curve section is significantly greater than that in the straight section. Under the same condition, the impact of the train on the PC track beam in the curve section is greater.
(5) According to ISO2631 and UIC513, the riding comfort of the monorail train is evaluated by the comfort and stability index. The results show that the monorail train has a good riding comfort.

Acknowledgments

The research was funded by the National Natural Science Foundation of China (Grant No. 51878563), the Sichuan Science and Technology Program (Grant No. 2018JY0294 and 2018JY0549), and the Ministry of Science and Technology of China (Grant No. KY201801005).

References

Altunisik, A.C. and Kalkan, E. (2016), "Investigation of earthquake angle effect on the seismic performance of steel bridges", *Steel Compos. Struct., Int. J.*, **22**(4), 855-874. http://dx.doi.org/10.12989/scs.2016.22.4.855

Androus, A., Afefy, H.M. and Sennah, K. (2017), "Investigation of free vibration and ultimate behavior of composite twin-box girder bridges", *J. Constr. Steel Res.*, **130**, 177-192. https://doi.org/10.1016/j.jcsr.2016.12.017

Caglayan, O., Ozakgul, K., Tezer, O. and Piroglu, F. (2015), "In-situ field measurements and numerical model identification of a multi-span steel railway bridge", *J. Test. Eval.*, **43**(6), 1323-1337. https://doi.org/10.1520/JTE20140049

Cui, C., Zhang, Q.H., Luo, Y., Hao, H. and Li, J. (2018a), "Fatigue reliability evaluation of deck-to rib welded joints in OSD considering stochastic traffic load and welding residual stress", *Int. J. Fatigue*, **111**, 151-160. https://doi.org/10.1016/j.ijfatigue.2018.02.021

Cui, C., Bu, Y.Z., Bao, Y., Zhang, Q.H. and Ye, Z. (2018b), "Strain energy-based fatigue life evaluation of deck-to-rib welded joints in OSD considering combined effects of stochastic traffic load and welded residual stress", *J. Bridge Eng.*, **23**(2), 04017127. https://doi.org/10.1061/(ASCE)BE.1943-5592.0001181

DBJ/T (2014), Technical specification for inspecting dynamic characteristic of bridge engineering structures. [In Chinese]

Deng, D., Huang, G.J. and Jiang, G.B. (2007), "Application of DEWE-BOOK data acquisition system and DASYLab configuration software", *Mech. Elec. Tech. Hydropower Sta.*, **30**(4), 24-26.

Goda, K., Nishigaito, T., Hiraishi, M. and Iwasaki, K. (2000), "A curving simulation for a monorail car", *Railroad Conference*, pp. 171-177. 10.1109/RRCON.2000.869998

Gou, H.Y., Shi, X.Y. and Zhou, W. (2018a), "Dynamic performance of continuous railway bridges: Numerical analyses and field tests", *Proc I Mech E, Part F: J. Rail Rapid Transit*, **232**(3), 936-955. https://doi.org/10.1177/0954409717702019

Gou, H.Y., Zhou, W., Yang, C.W., Bao, Y. and Pu, Q.H. (2018b), "Dynamic response of long-span concrete-filled steel tube tied arch bridge and riding comfort of monorail trains", *Appl. Sci.*, **8**(4), 650. https://doi.org/10.3390/app8040650

Gou, H.Y., He, Y.N., Zhou, W., Bao, Y. and Chen, G.D. (2018c), "Experimental and numerical investigations of the dynamic responses of an asymmetrical arch railway bridge", *Proc I Mech E, Part F: J. Rail Rapid Transit.*, **232**(9), 2309-2323.

Gou, H.Y., Zhou, W., Chen, G.D., Bao, Y. and Pu, Q.H. (2018d), "In-situ test and dynamic response of a double-deck tied-arch bridge", *Steel Compos. Struct., Int. J.*, **27**(2), 161-175. http://dx.doi.org/10.12989/scs.2018.27.2.161

Gou, H.Y., Zhou, W., Bao, Y., Li, X.B. and Pu, Q.H. (2018e), "Experimental Study on Dynamic Effects of a Long-span Railway Continuous Beam Bridge", *Appl. Sci.*, **8**(5), 669. DOI: 10.3390/app8050669

Gou, H.Y., Long, H., Bao, Y., Chen, G.D., Pu, Q.H. and Kang, R. (2018f), "Stress distributions in girder-arch-pier connections of long-span continuous rigid frame arch railway bridge", *J. Bridge Eng.*, **23**(7), 04018039. https://doi.org/10.1061/(ASCE)BE.1943-5592.0001250

Gou, H.Y., Wang, W., Shi, X.Y., Pu, Q.H. and Kang, R. (2018g), "Behavior of steel-concrete composite cable anchorage system", *Steel Compos. Struct., Int. J.*, **26**(1), 115-123. http://dx.doi.org/10.12989/scs.2018.26.1.115

Gou, H.Y., Long, H., Bao, Y., Chen, G.D. and Pu, Q.H. (2019), "Dynamic behavior of hybrid framed arch railway bridge under moving trains", *Struct. Infrastruct Eng.* 10.1080/15732479.2019.1594

Guo, W.H. and Xu, Y.L. (2001), "Fully computerized approach to

study cable-stayed bridge-vehicle interaction", *J. Sound Vib.*, **248**(4), 745-761. https://doi.org/10.1006/jsvi.2001.3828

Hogan, L.S., Wotherspoon, L., Beskhyroun, S. and Ingham, J. (2016), "Dynamic Field Testing of a Three-Span Precast-Concrete Bridge", *J. Bridge Eng.*, **21**(12), 06016007. https://doi.org/10.1061/(ASCE)BE.1943-5592.0000970

Huang, X.Y., Chen, Y.J. and Li, Y. (2010), "Influence of curvature radius on impact effects of a box-girder curved bridge under moving vehicle loads", *J. Vib. Shock*, **29**(1), 38-42.

ISO 2631-1 (1997), Mechanical Vibration and shock- Evaluation of human exposure to whole-body vibration- Part 1- General Requirements; Organization I S.

Ivanchenko, I.I. (2008), "Substructure method in high-speed monorail dynamic problems", *Mech. Solids*, **43**(6), 925-938. https://doi.org/10.3103/S002565440

Jerri, A.J. (2005), "The Shannon Sampling Theorem – Its Various Extensions and Applications: A Tutorial Review", *Proceedings of the IEEE*, **65**(11), 1565-1596.

Kashani, H. and Nobari, A.S. (2012), "Structural Nonlinearity Identification Using Perturbed Eigen Problem and ITD Modal Analysis Method", *Appl. Mech. Mater.*, **232**, 949-954. https://doi.org/10.4028/www.scientific.net/AMM.232.949

Kim, C.W. and Kawatani, M. (2006), "Effect of train dynamics on seismic response of steel monorail bridges under moderate ground motion", *Earthq. Eng. Struct. D.*, **35**(10), 1225-1245. https://doi.org/10.1002/eqe.580

Kim, C.W., Kawatani, M., Kanbara, T. and Nishimura, N. (2013), "Seismic behavior of steel monorail bridges under train load during strong earthquakes", *J. Earthq. Tsunami.*, **7**(2), 269-285. https://doi.org/10.1142/S1793431113500061

Kudu, F.N., Bayraktar, A. and Bakir, P.G. (2014), "Ambient vibration testing of Berta Highway Bridge with post-tension tendons", *Steel Compos. Struct., Int. J.*, **16**(1), 23-46. http://dx.doi.org/10.12989/scs.2014.16.1.023

Lee, C.H., Kim, C.W. and Kawatani, M. (2005), "Dynamic response analysis of monorail bridges under moving trains and riding comfort of trains", *Eng. Struct.*, **27**(14), 1999-2013. https://doi.org/10.1016/j.engstruct.2005.06.014

Lee, C.H., Kawatani, M. and Kim, C.W. (2006), "Dynamic response of a monorail steel bridge under a moving train", *J. Sound Vib.*, **294**(3), 562-579. https://doi.org/10.1016/j.jsv.2005.12.028

Liu, Y.Y., Ge, Y.M. and Yang, Y.R. (2010), "Vibration characteristic of coupled system for straddle type monorail beam and train", *J.Traffic Trans. Eng.*, **10**(2), 46-53.

Naeimi, M., Tatari, M. and Esmaeilzadeh, A. (2014), "Dynamic interaction of the monorail-bridge system using a combined finite element multibody-based model", *Proc I Mech E, Part K J. Multi-body Dynamics*, **229**(2), 132-151. https://doi.org/10.1177/1464419314551189

Naeimi, M., Tatari, M. and Esmaeilzadeh, A. (2015), "Dynamics of the Monorail Train Subjected to the Braking on a Straight Guideway Bridge", *Arch. Mech. Eng.*, **62**(3), 363-376. https://doi.org/10.1515/meceng-2015-0021

Peng, G., Deng, J., Liu, A. and Yu, Q. (2016), "Seismic performances of steel reinforced concrete bridge piers", *Steel Compos. Struct., Int. J.*, **21**(3), 661-677. http://dx.doi.org/10.12989/scs.2016.21.3.661

Railway Transport [2004] No. 120 (2004), Code for rating existing railway bridges; Chinese Railway Ministry, Beijing, China. [In Chinese]

Shan, D.S. and Li, Q. (2004), "Effect of Curvature Radii on Vehicle-Bridge Coupled Vibration about Continuous Curved Girder Bridges", *Bridge Const.*, **6**, 1-3.

Shi, Z., Chen, Y.C., Jiang, Y.T., Zhu, J., Pu, Q.H. and Gao, Y.F. (2016), "Bridge static load test deflection dial indicator measurement connection device", Chinese Patent CN205482765U.

Shibeshi, R.D. and Roth, C.P. (2016), "Field measurement and dynamic analysis of a steel truss railway bridge", *J. S. Afr. Civ. Eng.*, **58**(3), 28-36. http://dx.doi.org/10.17159/2309-8775/2016/v58n3a4

Song, Y.M., Wu, D.J. and Hou, Y.J. (2012), "Analysis of dynamics interaction about train curving bridge on small radius and reverse curve", *Eng. Mech.*, **29**, 185-189.

Song, Y.M., Wu, D.J. and Li, Q. (2017), "Experimental Study on Train-induced Vibration of Small Radius and Reverse Curve Bridge", *J. China Rail. Soc.*, **39**(9), 126-133.

Sun, H., Pang, H.R., Zhang, C. and Guo, X.Q. (2018), "Dynamic Characteristic Analysis of Vertical Lift Bascule Arch Bridge", *J. Arch. Civil Eng.*, **35**(1), 86-92.

Toydemir, B., Koçak, A., Sevim, B. and Zengin, B. (2017), "Ambient vibration testing and seismic performance of precast i beam bridges on a high-speed railway line", *Steel Compos. Struct., Int. J.*, **23**(5), 557-570. http://dx.doi.org/10.12989/scs.2017.23.5.557

Turker, T., Bayraktar, A., Altunisk, A.C. and Sevim, B. (2007), "Modal testing and finite element model calibration of an arch type steel footbridge", *Steel Compos. Struct., Int. J.*, **7**(6), 487-502. http://dx.doi.org/10.12989/scs.2007.7.6.487

UIC code 513 (1994), Guidelines for evaluating passenger comfort in relation to vibration in railway vehicles, International Union of Railways.

Votsis, R.A., Stratford, T.J. and Chryssanthopoulos, M.K. (2017), "Dynamic assessment of a FRP suspension footbridge through field testing and finite element modelling", *Steel Compos. Struct., Int. J.*, **23**(2), 205-215. http://dx.doi.org/10.12989/scs.2017.23.2.205

Wang, S.Q. (2004), "Characteristics of straddle type monorail railway and its application prospects", *China Rail Sci.*, **25**(1), 131-135.

Wang, H.L. and Zhu, E.Y. (2018), "Dynamic response analysis of monorail steel-concrete composite beam-train interaction system considering slip effect", *Eng. Struct.*, **160**, 257-269. https://doi.org/10.1016/j.engstruct.2018.01.037

Wang, F.C., Xu, Y.L., Wang, C.Y., Liu, T.G. and Liu, F.Q. (2011), "Experimental study on composite foundation with rubberized cement-soil pile under horizontal load", *J. Shenyang Jianzhu University*, **27**(6), 1115-1120.

Wang, S.Q., Peng, P.H., Yang, Z., Ma, Q. and Zhang, T. (2018), "Coupling vibration analysis of passenger-vehicle-bridge system", *J. Vib. Eng.*, **31**(1), 30-38.

Zhai, W.M. (2015), *Vehicle-track coupled dynamics*, China Science Publishing & Media Ltd., Beijing, China. [In Chinese]

Zhong, M.L. and Zhu, E.Y. (2013), "Development of emergency track beam alignment for rapid track beam replacement of straddle monorail transit", *J. Transp. Eng.*, **139**(4), 416-423. https://doi.org/10.1061/(ASCE)TE.1943-5436.0000497

CC